Power Electronic Systems
Laboratory



IEEE Transactions on Industry Applications, Vol. 60, No. 1, pp 321-331, February 2024

# Magnetically Self-Bearing Drive System for Ultracentrifugation: towards 100’000 rpm and 200’000 g

E. Hubmann,
R. Eberhard,
C. Blaser,
S. Erismann,
D. Steinert,
T. Nussbaumer,
J. W. Kolar



ETH zürich

This article has been accepted for publication in IEEE Transactions on Industry Applications. This is the author's version which has not been fully edited and content may change prior to final publication. Citation information: DOI 10.1109/TIA.2023.3314016

# Magnetically Self-Bearing Drive System for Ultracentrifugation: Towards 100'000 rpm and 200'000 g

E.J. Hubmann*, R. Eberhard*, C.F. Blaser*, S. Erismann*, D. Steinert†, T. Nussbaumer†, J. W. Kolar*
*Power Electronic Systems Laboratory ETH Zurich, Switzerland, hubmann@lem.ee.ethz.ch
†Levitronix GmbH Zurich, Switzerland, steinert@levitronix.com

***Abstract*—A novel magnetically double self-bearing drive system for ultracentrifugation in pharmaceutical and chemical industry is presented, built as a prototype and operated. The prototype successfully reached its operating speed of $100'000\,\mathrm{rpm}$. It features an opening stator functionality allowing for fast removal of the ultracentrifuge rotor while enabling future centrifugal acceleration levels of $200'000\,\mathrm{g}$. The openable stators require a stator encapsulation, provoking unavoidable stator yoke air-gaps. Parasitic induced phase-currents were identified, a current-control strategy proposed to diminish them and successfully implemented and operated on the prototype.**

***Index Terms*—self-bearing motor, high-speed, control**

## I. Introduction

In biochemistry, fundamental processes are the separation of components of heterogeneous mixtures and purification with ultracentrifuges. Typical ultracentrifuge rotors today are mechanically suspended. Mechanical suspension at high speeds impairs rotor accessibility, requires complicated sealing, causes bearing losses, requires lubrication, generates wear, poses a contamination risk and leads to limited life-time or maintenance needs. These are all limitations of the current technology applied in industry. In [1], the feasibility of a novel system solving these problems was conceptually shown. This article now presents the new fully established working hardware. Furthermore, solutions to problems and challenges related to current control and rotor dynamics which were not yet anticipated in [1] are shown.

In [2], a magnetic levitation based continuous flow ultracentrifuge (UCF) prototype was presented, reaching a centrifugal acceleration $C$ of up to $C = 10^5 g$ and a flow rate of $Q = 0.4\,\mathrm{L/min}$ with a rotational speed higher than $64\,\mathrm{krpm}$. However, the access to the UCF rotor for e.g. cleaning is difficult for the operators due to the self-bearing motor stators fully enclosing it.

This article presents a novel magnetically self-bearing openable drive system, omitting these limitations.

**Fig. 1** shows a conceptual illustration thereof. Two self-bearing motors (SBMs), forming a double self-bearing motor, drive the UCF rotor and keep it contact-less in place. As a special feature, a joint between the self-bearing motor modules allows access to the rotor and simple insertion or removal thereof.

Compared to modularly assembled stators during motor manufacturing (e.g. shown in [3]), which are and remain inevitably closed after assembly, the presented self-bearing motors need to be openable by the UCF operators in industry.

This article presents a new hardware UCF drive-system prototype fulfilling the target performance for the industrial UCF application. It furthermore presents solutions to the faced technical challenges in the previously unknown current control strategy of novel openable motors and the rotor-dynamics of the UCF.

In **Fig. 2(a)** the realized prototype of the double self-bearing UCF drive system is shown. It is in the closed ready-to-operate state. **Fig. 2(b)** shows the unique novel ability to unfold in an open state for removal or replacement of the UCF rotor. The indicated system dimensions in **Fig. 2** are specified in **Tab. I**

This article is structured as follows. In **Sec. II**, two key design challenges are discussed: on the one hand the requirement to have a stator that can be opened and on the other hand the requirement to realize a rotor with bending resonance frequencies above $100\,\mathrm{krpm}$, outside the speed operating range. In **Sec. III**, the topology choice and its working principle is explained. In **Sec. IV**, the realized motor prototype is presented, and a fundamental challenge for novel openable

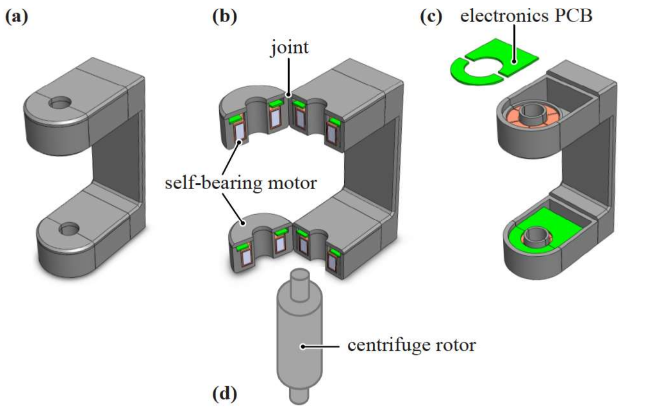


**Fig. 1:** **(a)** Conceptual illustration from [1] of the novel magnetically self-bearing drive system for the targeted $100'000\,\mathrm{rpm}$ and $200'000\,\mathrm{g}$ ultracentrifugation. **(b)** Accessible ultracentrifuge rotor for insertion or removal by operators. **(c)** Possible placement of the power electronics. **(d)** Conceptual illustration of the ultracentrifuge rotor.

This article has been accepted for publication in IEEE Transactions on Industry Applications. This is the author's version which has not been fully edited and content may change prior to final publication. Citation information: DOI 10.1109/TIA.2023.3314016

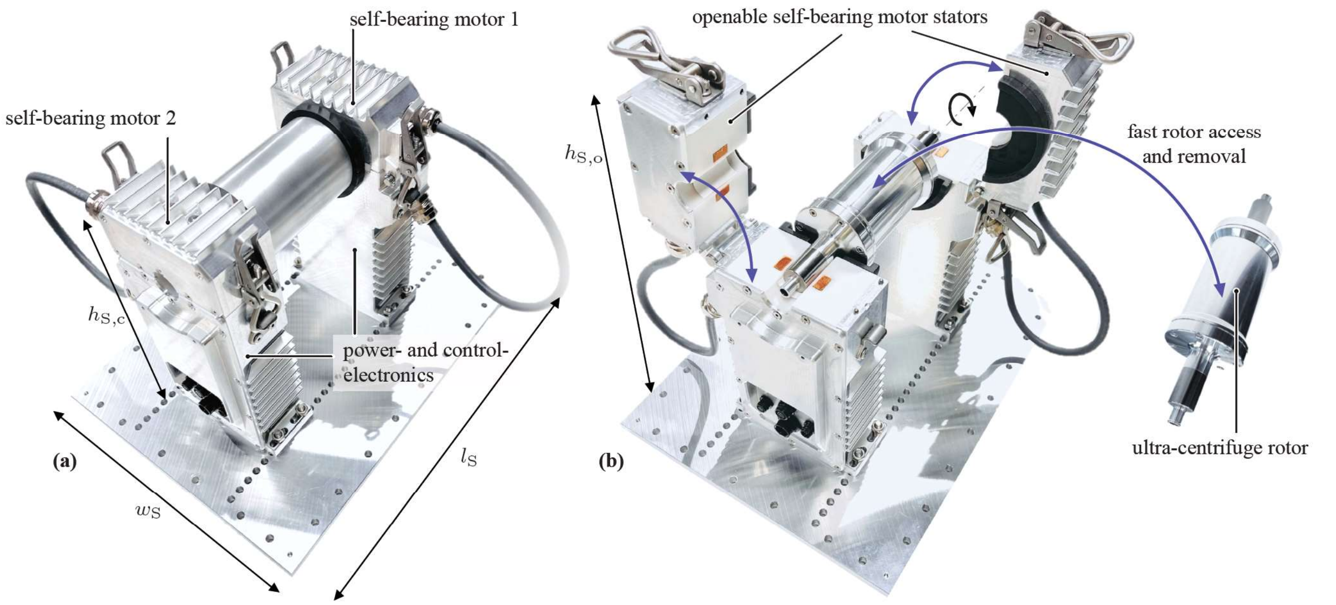


**Fig. 2: (a)** Dual self-bearing motor ultracentrifuge drive system prototype in closed ready-to-operate state. **(b)** Unique novel self-bearing motors being able to unfold into an open state for removal or replacement of the ultracentrifuge rotor by operators. (Indicated system dimensions specified in **Tab. I**).

motors unveiled. Necessary encapsulation of the stator halves leads to unavoidable yoke air-gaps. The occurrence of resulting flux variations in the stator during operation causes parasitic phase-currents. Therefore, the usage of an $L-$filter and a voltage feed-forward compensation current control scheme is proposed. In **Sec. V**, the rotor bending resonances are investigated and sub-critical rotor behavior is shown using 3D-FEM simulation and an acoustic impulse response experiment. The new UCF drive system prototype was successfully commissioned and operated with the proposed current control scheme up to $103'000\,\mathrm{rpm}$. An experimental proof of that high-speed operation and the working of the proposed control method is shown in **Sec. VI**. The findings are finally summarized in **Sec. VII** and an outlook is provided.

## II. Key System Design Challenges

In [1], the competing system design relationships for a drive system for UCF application were revealed. On the one hand, the rotor diameter of the UCF and its operating speed must be selected such that the desired centrifugal acceleration is achieved ($200'000\,\mathrm{g}$ in this article). On the other hand, the drive system must be able to provide necessary mechanical power to the rotor to overcome the air friction losses resulting from the rotor speed, diameter and length. The denser the rotor material, the higher the material load and thus its strength requirement. The rotor material must therefore have a suitable combination of low material density and high strength. In turn, the rotor design must have sufficiently high bending resonance frequencies, determined by the weight and stiffness combination, such that they are not excited during operation.

In the following, the two key challenges are highlighted: on the one hand the requirement for the self-bearing drive system to have an openable stator, on the other hand, the requirement for a sub-critical rotor design for the target speed of $100\,\mathrm{krpm}$.

### A. Self-Bearing Motor Opening-Capability

To allow for fast insertion and removal of the UCF rotor by operators in an industrial manufacturing plant, the novel UCF drive-system requires a stator which is split in two separate segments and therefore can be mechanically opened as shown in **Fig. 3(a)**.

While open, the stator-halve interface is exposed to the outside production facility/laboratory-environmental conditions. It therefore must be protected from external influences such as contact with process fluids, cleaning agents or unintentional mechanical impacts. Especially the stator core requires special protection. For this purpose, a $0.1\,\mathrm{mm}$ thick protective paint coating is envisaged on the exposed stator core separation surfaces. Such a coating behaves magnetically like air, and is therefore referred to in the following as a yoke air-gap in a magnetic sense.

Due to this, in total $0.2\,\mathrm{mm}$ thin, yoke air-gap in the stator separation plane, harmonic field content is introduced, and the current control needs to be able to counteract resulting induced voltage harmonics.

### B. Rotor Dynamics

To avoid excessive vibration or instabilities of the magnetically levitated rotor, the first (and thus lowest) rotor bending resonance frequency, as shown in **Fig. 3(b)**, should be above the maximum frequency of the rotational speed (sub-critical operation). However, higher order synchronous excitations will hit rotor bending modes, and the resulting rotor resonance behavior needs to be stabilized by the control system. The control scheme must furthermore be capable of operating the

This article has been accepted for publication in IEEE Transactions on Industry Applications. This is the author's version which has not been fully edited and content may change prior to final publication. Citation information: DOI 10.1109/TIA.2023.3314016

novel UCF drive system, despite its new unique properties, including yoke air-gaps in the stator magnetic circuit, which is shown in **Sec. IV**.

Summarizing, specific design is needed both for the motor as described in **Sec. III**, **Sec. IV**, and for the rotor as presented in **Sec. V**, the validation is in **Sec. VI**.

## III. Slotless Double Self-Bearing Openable Motor

Self-bearing motors (SBMs) have the unique capability of taking over both the driving and magnetic bearing functionality. This simplifies the drive system architecture, as no separate magnetic bearing units are required.

A wide range of SBM applications and accordingly specialized technical solutions are reported in literature. In [4] an overview over the current state of the technology of SBMs with significant power output is provided. A review of the working principles and topologies of SBMs is published in [5].

The field of SBM research is very active. Current trends include reduction of permanent magnet material usage [6] and new SBM topologies to reduce the complexity of the needed power electronics [7]- [9]. Earlier SBMs had typically separate winding sets for bearing force and torque generation. For combined winding topologies as used in this article, current research addresses their design and operation [10], optimal current utilization strategies [11] and new parallel winding topologies [12]- [15]. General SBM design-guidelines were recently proposed e.g. in [16]- [17], control strategies are active research topics as well, with e.g. [18] investigating the passing through critical speeds and [19] investigating state observers to improve position control. The field of high-speed SBMs experiences continuous attention with recent publications of systems operating at $30\,\mathrm{krpm}$ of [20] and [21], at $60\,\mathrm{krpm}$ of [22] and at $100\,\mathrm{krpm}$ of [23], [24].

However, to the authors' knowledge, the possibility to open high-speed SBM stators in the industrial application by operators, leading to unavoidable yoke air-gaps and their implications on the control, was not reported in literature so far. These aspects are therefore investigated in the following.

### A. Topology for UCF Openable SBMs

For the desired UCF application with openable SBM stators, the topology of slotless SBMs with combined windings in toroidal realization as shown in **Fig. 4** exhibits several advantages. It allows for the separation of the stator in two separate stator modules.

Furthermore, it leads to a low general and especially rotor loss potential for very high speeds. In contrast, the typical high rotor losses of slotted designs at very high speeds are caused by stronger and higher order harmonics in the air-gap field due to the teeth interaction with the field [25], [26]. Slotless SBMs can exhibit an almost sinusoidal air-gap field for the rotor pole-pair number $p = 1$ [27], which is ideal for highspeed applications with low rotor losses. It results in very low harmonic field content, and $p = 1$ leads to the lowest possible fundamental electrical frequency for a given mechanical speed. This results again in low losses. Therefore for openable UCF SBMs, a slotless stator topology with rotor pole pair number equal to one is very promising.

In SBMs, drive and bearing currents create fields in the same air-gap. The magnetic bearing forces can either be generated with the aid of separate bearing windings, or with the aid of a mathematical superposition of bearing and drive currents in combined windings, as shown in e.g. [28]. The stator field and related forces acting on the rotor are created by superimposed currents of drive and bearing action as shown in e.g. [29]. Combined windings for bearing forces and torque generation lead to equal loading of all coils and full utilization of the winding copper cross-section. If the bearing currents were in separate bearing coil sets, this would not be the case. Therefore, also all semiconductors of the connected power electronics benefit from equal current loading. Additionally, in [27] it was shown that the usage of combined windings lowers the higher order field harmonics induced by the stator drive and bearing currents, additionally reducing the current induced losses at high speeds.

In **Fig. 4(d)** the winding scheme of the resulting UCFs SBM topology is presented. It consists of two three-phase systems $a$ and $b$ with phase connections $u_\mathrm{a}$, $v_\mathrm{a}$, $w_\mathrm{a}$ and $u_\mathrm{b}$, $v_\mathrm{b}$, $w_\mathrm{b}$ respectively. The two three-phase systems are star-connected at the star-points $Y_\mathrm{a}$ and $Y_\mathrm{b}$ respectively.

To electrically connect the fixed and the movable stator module in **Fig. 4(c)**, a flexible cable connection with a high enough bending radius for repeated bending is envisaged **Fig. 4(d)**.

### B. Self-Bearing Motor Working Principle

In **Fig. 4** the working principle for the UCF SBM torque **(a)** and force generation **(b)** is shown. For the torque generation, in **Fig. 4(a)**, a stator field with the same pole-pair number as the rotor is generated commonly with all six windings. It is $90°$ ahead of the rotor's permanent magnet field, which leads to torque generation. To create bearing forces as shown in **Fig. 4(b)**, the same six windings generate a two-pole pair stator field which generates together with the rotor field bearing forces with controllable amplitude and direction.

## IV. Self-Bearing Motor With Yoke Air-Gaps

**Fig. 5(a)** shows the stator halves with soft magnetic composite (SMC) cores of one of the realized $100\,\mathrm{krpm}$ $48\,\mathrm{V_{DC}}$ fed $0.25\,\mathrm{kW}$ (each) drive system prototypes of the previously discussed topology for UCF application. The main UCF SBM prototype specifications are listed in **Tab. II** and the used materials of the prototype in **Tab. III**.

### A. Yoke Air-Gap Induced Flux Variation

In **Fig. 5(b)** a 3D-FEM electromagnetic simulation of the magnetic flux density is shown. The yoke air-gaps introduce harmonic field content as shown in **Fig. 5(b1)**-**(b2)**, due to reduced reluctance for $\varphi = \{0, \pi\}$ with no flux crossing over

This article has been accepted for publication in IEEE Transactions on Industry Applications. This is the author's version which has not been fully edited and content may change prior to final publication. Citation information: DOI 10.1109/TIA.2023.3314016

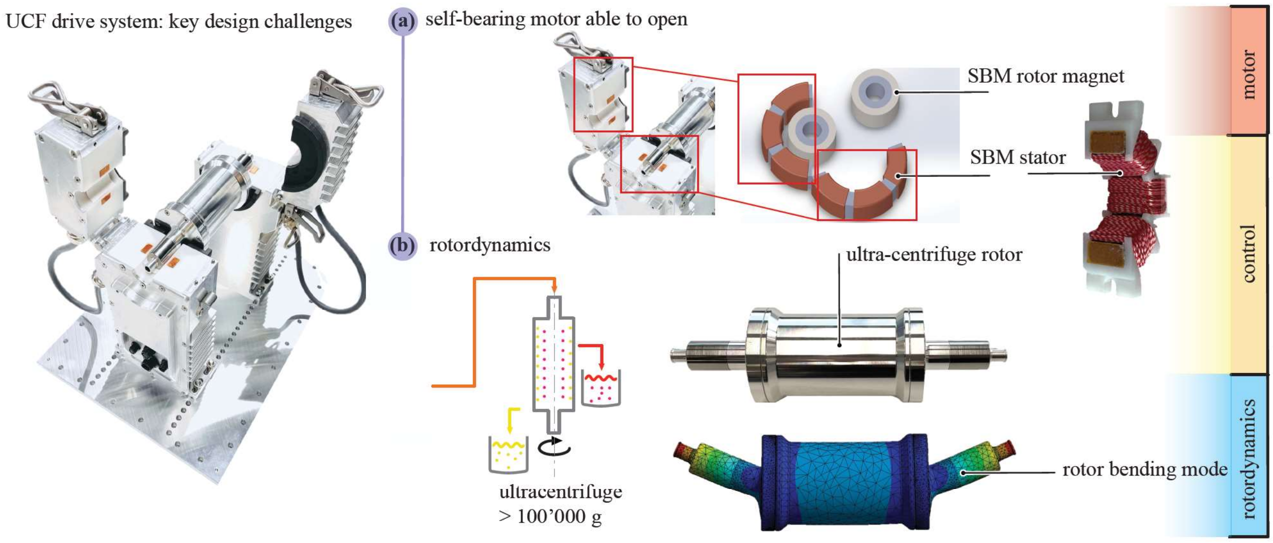


**Fig. 3:** Key design challenges: **(a)** Openable stator for good access to the rotor by UCF operators. Necessary encapsulation of the stator for protection against environmental influences. This leads to unavoidable interruption of the magnetic circuit with corresponding problems for the current-control. **(b)** Rotor design such that the first bending mode can never be excited by frequencies corresponding to the rotational speed.

the yoke air-gaps, and increased reluctance with flux crossing over the yoke air-gap for $\varphi = \{\pi/2, -\pi/2\}$.

The resulting linked rotor permanent magnet fluxes $\phi_1 - \phi_6$ in the six coils (per turn) are shown in **Fig. 5(c)**. The center coils 2 and 5 of the stator limbs experience a slightly higher flux amplitude increased by $\phi_\Delta$. The flux in each phase can therefore be stated as:

$$\begin{aligned} \phi_\mathrm{u}(t) &= \left(\hat{\phi} + \phi_\Delta\right) \cdot \cos\left(p\Omega t\right) \\ \phi_\mathrm{v}(t) &= \hat{\phi} \cdot \cos\left(p\Omega t - \frac{2\pi}{3}\right) \\ \phi_\mathrm{w}(t) &= \hat{\phi} \cdot \cos\left(p\Omega t + \frac{2\pi}{3}\right) , \end{aligned} \tag{1}$$

where $\Omega$ stands for the rotational speed.

**Fig. 5(d)** shows the $dq$-transformed fluxes. Both $d$- and $q$-flux show a second harmonic flux variation with approx. $4\,\%$ of the $d$-flux amplitude, as also analytically can be shown by applying the $dq$-transform on the previous equations, on the one hand for the $d$-component:

$$\begin{aligned} \frac{3}{2}\phi_\mathrm{d}(t) &= \frac{3}{2}\hat{\phi} + \phi_\Delta \cdot \cos^2\left(p\Omega t\right) \\ &= \frac{3}{2}\hat{\phi} + \frac{1}{2}\phi_\Delta + \frac{1}{2}\phi_\Delta \cdot \cos\left(2p\Omega t\right) \end{aligned} \tag{2}$$

and similarly for the $q$-component:

$$\begin{aligned} \frac{3}{2}\phi_\mathrm{q}(t) &= \phi_\Delta \cdot \cos\left(p\Omega t\right) \cdot \sin\left(p\Omega t\right) \\ &= -\frac{1}{2}\phi_\Delta \cdot \sin\left(2p\Omega t\right) \\ &= \frac{1}{2}\phi_\Delta \cdot \cos\left(2p\Omega t - \frac{\pi}{2}\right) . \end{aligned} \tag{3}$$

By extracting the time-varying parts of the $dq$-fluxes $\phi_{\mathrm{d},\Delta}(t)$ and $\phi_{\mathrm{q},\Delta}(t)$:

$$\begin{aligned} \phi_{\mathrm{d},\Delta}(t) &= \frac{1}{3}\phi_\Delta \cdot \cos\left(2p\Omega t\right) \\ \phi_{\mathrm{q},\Delta}(t) &= \frac{1}{3}\phi_\Delta \cdot \cos\left(2p\Omega t - \frac{\pi}{2}\right) , \end{aligned} \tag{4}$$

it is revealed that these time varying components both share the same amplitude, and show the same twofold frequency compared to the rotational speed $\Omega$. They create a 2D-circle in the $dq$-plane. The same result can be seen by transforming the 3D-FEM obtained fluxes to the $dq$-plane. It leads to a rotating flux variation space vector $\underline{\phi}_\Delta$, presented in **Fig. 5(e)**.

In the following, the implications, problems and a solution to the discovered flux variation in SBMs with yoke air-gaps are unveiled. The presented current-control solution is also realized in the hardware prototype.

### B. *Parasitic Induced Rotating Current and L-Filter Impact*

The separation of the stator into two halves for the stator opening-functionality leads to a parasitic magnetic flux variation. It shows three times the rotational frequency in the stationary frame of reference, and in the moving $dq$-frame of reference two times the rotational frequency. This leads to an induced voltage space vector $\underline{U}_\mathrm{g}$ of corresponding frequency. An equivalent circuit of the stator incorporating $\underline{U}_\mathrm{g}$ is shown in **Fig. 7(a)**.

The parasitic induced voltage amplitude $|\underline{U}_\mathrm{g}|$ can be written as:

$$|\underline{U}_\mathrm{g}| = p \cdot N \cdot \phi_\Delta \cdot \Omega. \tag{5}$$

Without further measures, $\underline{U}_\mathrm{g}$ leads to a parasitic current space vector $\underline{I}_\mathrm{g}$ rotating with the same frequency as $\underline{U}_\mathrm{g}$ as shown in the space vector diagram **Fig. 7(b)**. $\underline{U}_\mathrm{g}$ therefore leads to

This article has been accepted for publication in IEEE Transactions on Industry Applications. This is the author's version which has not been fully edited and content may change prior to final publication. Citation information: DOI 10.1109/TIA.2023.3314016

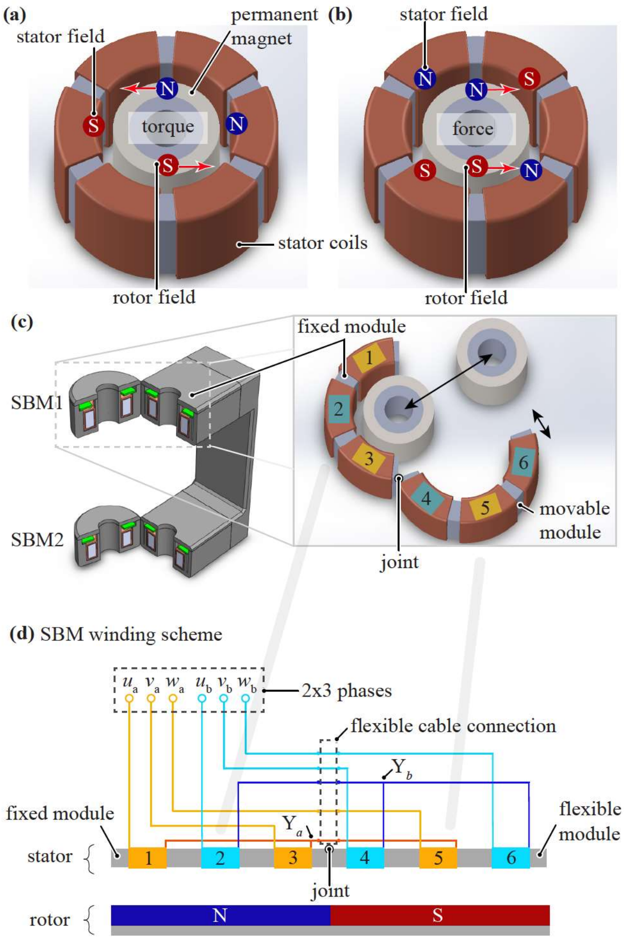


**Fig. 4:** From [1]: working principle of the slotless SBMs: **(a)** driving torque, and **(b)** bearing force generation. **(c)** Possibility to open the stators of the proposed UCF SBMs enabling access and removal of the UCF rotor. **(d)** SBM winding scheme of the proposed topology.

parasitic $d$- and $q$-currents. In the space vector diagram, the voltage drop across the stator resistance $R_\mathrm{S}$ is neglected, as for high efficiency motors $|\underline{U}_\mathrm{p}| >> |\underline{U}_\mathrm{R}|$. The parasitic current amplitude $|\underline{I}_\mathrm{g}|$ calculates as:

$$|\underline{I}_\mathrm{g}| = \frac{p \cdot N \cdot \phi_\Delta \cdot \Omega}{\sqrt{R_\mathrm{s}^2 + (3\Omega)^2 \cdot L_\mathrm{d}^2}}. \tag{6}$$

At low rotational speeds, its amplitude $|\underline{I}_\mathrm{g}|$ is limited by the stator resistance $R_\mathrm{S}$ to an initially linear rise with the speed. At high speeds, it is limited by the motor inductance $L_\mathrm{d}$ (rotor is non-salient, i.e. $L_\mathrm{d}$=$L_\mathrm{q}$) consisting of an optional phase $L$-filter inductance $L_\mathrm{f}$ and the stator synchronous inductance $L_\mathrm{S}$, with $L_\mathrm{d} = L_\mathrm{F} + L_\mathrm{S}$.

$$|\underline{I}_\mathrm{g}| = \frac{p \cdot N \cdot \phi_\Delta \cdot \Omega}{\sqrt{R_\mathrm{s}^2 + (3\Omega)^2 \cdot (L_\mathrm{F} + L_\mathrm{S})^2}}. \tag{7}$$

For high speeds, the parasitic current amplitude $|\underline{I}_\mathrm{g}|$ tends asymptotically towards the finite value $|\underline{I}_\mathrm{g,lim}|$:

$$|\underline{I}_\mathrm{g,lim}| = \frac{p \cdot N \cdot \phi_\Delta}{3\,(\cdot L_\mathrm{F} + L_\mathrm{S})}. \tag{8}$$

If the stator winding synchronous inductance $L_\mathrm{S}$ is very low, as it is usually the case with high-speed motors, the parasitic current amplitude $|\underline{I}_\mathrm{g}|$ can assume large values without additional filter inductances $L_\mathrm{F}$.

**Fig. 6** shows for the UCF SBMs of this article the analytically calculated parasitic current amplitude $|\underline{I}_\mathrm{g}|$ based on **Eq. 7** for a relative flux variation w.r.t. the $d$-flux amplitude of $4\,\%$. It is shown once without $L$-filter and once with a filter inductance of $L_\mathrm{F} = 3 \cdot L_\mathrm{S}$. It should be noted, that in the shown 3D-FEM simulation in **Fig. 5(b)**, a perfectly manufactured yoke air-gap geometry is assumed. In a real hardware, especially for SMC stator material, the stator edges are imperfect, or need to be rounded slightly, thus increasing the effective yoke air-gap and therefore also the parasitic induced currents $\underline{I}_\mathrm{g}$, especially for small motors where the non-ideal edge geometry has an even larger influence.

### C. Yoke Air-Gap Design

To allow the opening of the SBMs by the industrial operators, the stators are separated in two halves. Necessary protective coating leads unavoidably to at least two yoke air-gaps.

From a magnetic standpoint, it seems attractive to place three yoke air-gaps offset by 120° each to achieve a symmetry w.r.t. the three-phase winding. However, the cost and complexity of an industrial system with three stator units, each of them encapsulated and connected by shielded cables leads to the preference of only one separation plane. Additionally, each introduced air-gap increases the unwanted stator reluctance.

The yoke air-gaps should be kept as thin as possible, to reduce adverse effects. However, appropriate durable coating for an industrial environment will always require a certain thickness.

To further reduce the effect of the yoke air-gap between the stator halves, geometric measures are conceivable in the future. On the one hand, the area over which the magnetic flux is transmitted between the stator halves could be increased. On the other hand, if not all coils require the same number of turns for production reasons, the middle coil of each stator segment can have a slightly lower number of turns in order to have the same amount of linked flux in all coils. However, an exact matching, also due to tolerances, seems unlikely. Therefore a current control strategy is always needed.

### D. Adverse Effects of Parasitic Induced Rotating Current

The parasitic induced current $\underline{I}_\mathrm{g}$ generates a parasitic stator field with pole pair number $p = 1$, rotating with a frequency of $3 \cdot \Omega$ in the stator frame of reference, i.e. an asynchronous field. The self-bearing motors of this article generate bearing fields with number of bearing poles $P_\mathrm{bng} = P_\mathrm{drv} + 2 = p \cdot 2 + 2 = 4$. They are therefore according to [30] of type $P_\mathrm{bng} = P_\mathrm{drv} \pm 2$. This implies, that the parasitic field cannot generate

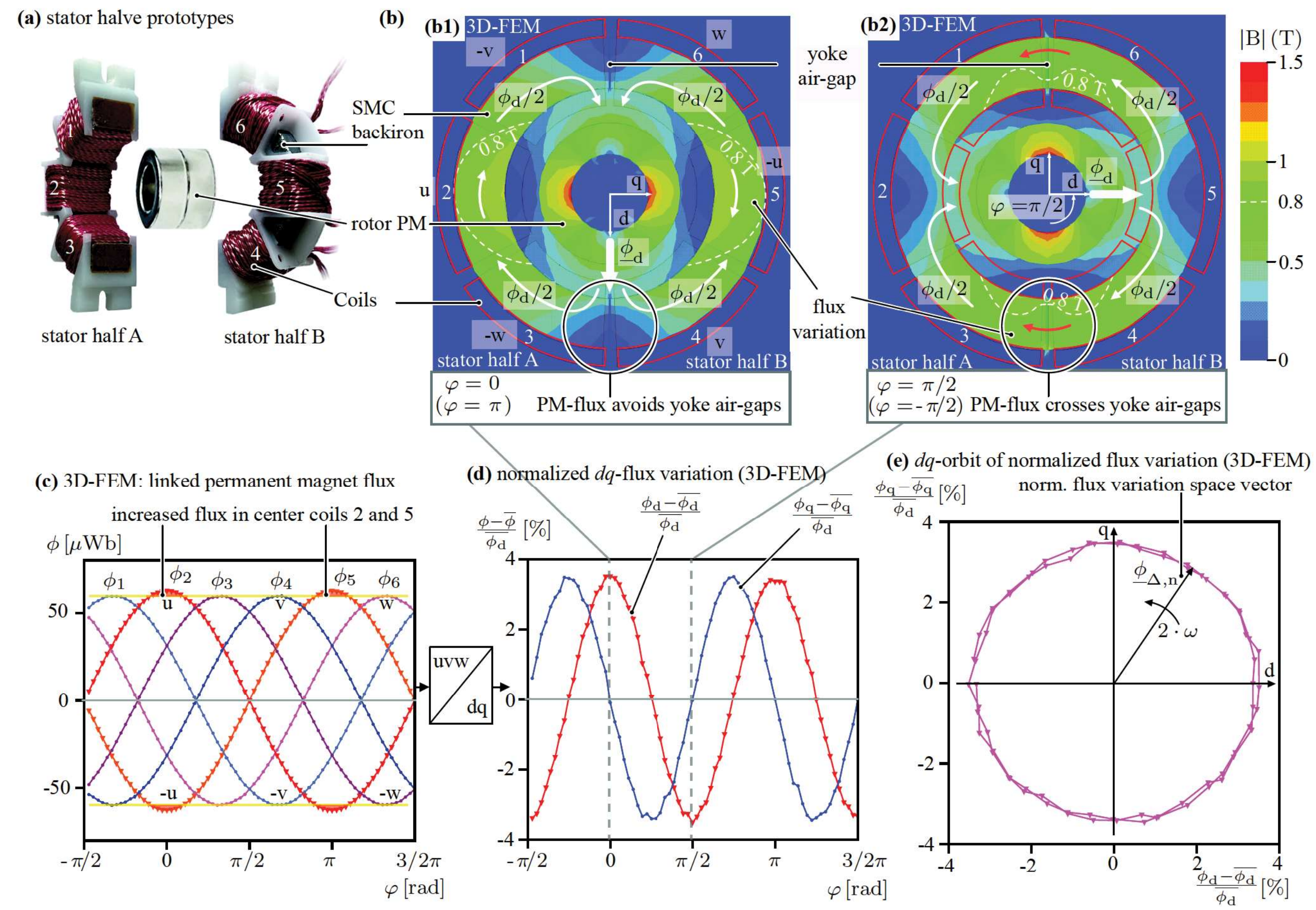


**Fig. 5:** **(a)** Stator of the realized double self-bearing slotless openable motor prototype. **(b)** 3D-FEM magnetic field simulation of the prototype motors. Thin yoke air-gaps for durable anti corrosion coating ($0.1\,\mathrm{mm}$ on each side) in the separation plane. Resulting yoke air-gap introduced harmonic field content **(b1)-(b2)**, due to increased reluctance and flux crossing for $\varphi = 0, \pi$ and reduced reluctance for $\varphi = \pi/2,\, 3/4\pi$. **(c)** Resulting linked rotor permanent magnet fluxes $\phi_1 - \phi_6$ in the six coils (per turn). **(d)** Transformed to $dq$-quantities, both $d$- and $q$-flux show a second harmonic flux variation with approx. $4\,\%$ of the $d$-flux amplitude. **(e)** In $dq$-plane this leads to a rotating flux variation space vector.

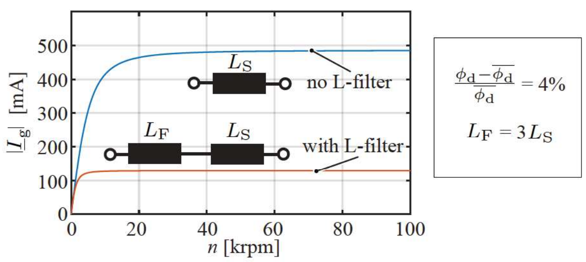


**Fig. 6:** Analytically calculated parasitic current amplitude $|\underline{I}_g|$ for the self-bearing motors of this article given a relative flux variation w.r.t. the $d$-flux amplitude of $4\,\%$ once without $L$-filter and once with a filter inductance of $L_F = 3 \cdot L_S$.

parasitic bearing forces. However parasitic torque ripple $\hat{T}_{Ig}$ of the frequency $2 \cdot \Omega$ is generated. The resulting speed ripple amplitude $\hat{\Omega}_{Ig}$ is kept limited by the rotor inertia $J$ as $\dot{\Omega} = T/J$ and increasingly attenuated with increasing speed $\Omega$ by the PI-speed control with low-pass closed-loop characteristic. For the envisaged UCF application, the speed ripple should be as small as possible to avoid re-mixing of the separated media.

$\underline{I}_g$ furthermore creates additional parasitic motor losses. On the one hand, $\underline{I}_g$ causes additional SMC stator core and rotor losses due to the asynchronous parasitic stator field (with an angular frequency of $3 \cdot \Omega$ in the stator frame of reference). On the other hand, additional copper losses in the windings are generated.

Compared to the rotor PM-field, the parasitic stator field is of less strength, but its threefold frequency of $3 \cdot \Omega$ implies, that SMC core loss terms from the Steinmetz equation [31] with quadratic frequency dependence are multiplied by $9 \cdot \Omega^2$. Furthermore the parasitic field is superimposed to the rotor PM-field and the stator fields for torque and bearing force generation. Thus, the parasitic field is added on top, increasing the loss generation potential, as the core losses are non-linear with the flux density and sensitive to field bias [32]. A detailed investigation of the complex mechanisms of this loss generation would go beyond the scope of this article and may be subject of future work. This article focuses instead on the root cause of $\underline{I}_\mathrm{g}$ and presents and experimentally validates a first approach to mitigate it.

### *E. Yoke Air-Gap Parasitic Current Feed-forward Control*

A voltage compensation by feed-forward control of the parasitic induced voltage $\underline{U}_\mathrm{g}$ on the nominal applied stator voltage $\underline{U}_\mathrm{s,nom}$ is proposed as shown in **Fig. 7(c)** and implemented on the presented prototype. The corresponding control circuit diagram is shown in **Fig. 8**.

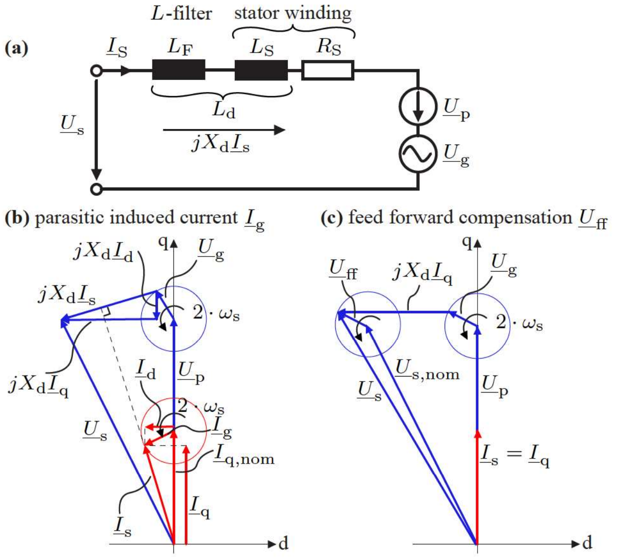

**Fig. 7:** **(a)** Stator equivalent electric circuit with parasitic induced voltage $\underline{U}_\mathrm{g}$ due to yoke-air-gap flux variation. **(b)** Space vector diagram with resulting current harmonics $\underline{I}_\mathrm{g}$. **(c)** Proposed feed-forward voltage space vector $\underline{U}_\mathrm{ff}$ compensation.

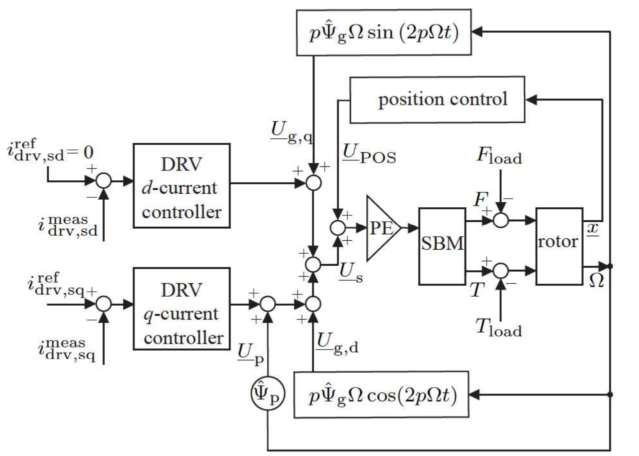

**Fig. 8:** Proposed current control scheme for the self-bearing openable motors with feed-forward control of the parasitic induced voltage $\underline{U}_\mathrm{g}$. The power electronics (PE) apply the resulting voltages from drive current-control and position-control to the combined windings of the SBMs.

With the presented voltage feed-forward current control strategy, the adverse effects of the yoke air-gaps can be counteracted.

## V. Rotor Dynamics

The conceptual feasibility of an UCF rotor for the drive system presented in this article was shown in [1]. The continuing step from concept to prototype taken in this article requires an investigation of the rotordynamics behavior of the actual design.

Compared to the rotor stiffness, the magnetic bearing stiffness is very small. Therefore, as an analytic approximation for the bending modes, the unsupported free vibration of a Euler-Bernoulli beam can be applied. The first bending mode resonance frequency $f_\mathrm{res,1}$ of a freely vibrating Euler-Bernoulli beam according to [34] is

$$f_\mathrm{res,1} = \frac{22.37}{2\pi L^2}\sqrt{\frac{E\cdot I_x}{\rho\cdot A}}\,, \tag{9}$$

with the length $L$, Young's modulus $E$, second moment of area $I_x$, density $\rho$ and cross-section $A$. The rotor is modeled as an annulus with inner and outer radii $r_1$ and $r_2$ and thickness $t = r_2 - r_1$. With the second moment of area $I_x$ of

$$I_x = \frac{\pi}{4}(r_2^4 - r_1^4)\,, \tag{10}$$

$f_\mathrm{res,1}$ can be rewritten as

$$f_\mathrm{res,1} = \frac{22.37}{2\pi L^2}\sqrt{\frac{E}{\rho}\cdot\frac{(r_1+t)^2+r_1^2}{4}}\,. \tag{11}$$

To achieve a high $f_\mathrm{res,1}$, a short rotor length $L$, high Young's modulus $E$, low density $\rho$, large inner radius $r_1$ and large thickness $t$ (for given $r_1$) are beneficial. Therefore these parameters can be varied and the rotor material chosen accordingly, in alignment with the rotor strength and air friction power consumption constraints, as shown in [1]. Knowing these influences, 3D-FEM rotor dynamics simulations can be performed in iterative manner until the desired $f_\mathrm{res,1}$ is achieved.

Within the scope of this article, two rotor designs were investigated. On the one hand, a test rotor shown in **Fig. 9(a1)** was designed to verify the drive system with respect to magnetically self-bearing and drive functionality. On the other hand, an UCF rotor prototype displayed in **Fig. 9(a2)** was designed to prove that the rotordynamic UCF requirements can be fulfilled. The rotor dimensions of both rotors are specified in **Tab. IV**.

For this purpose, 3D-FEM rotor dynamic simulations of the rotor bending modes were performed for both rotors and presented in Campbell diagrams in **Fig. 9(b1)** and **Fig. 9(b2)** respectively. For both rotors, in the speed operating range, the first bending resonance is above the synchronous first-order excitations (EO = 1) and thus, it is not excited by them during operation. Excitations of higher order (EO > 1) can in principle excite bending modes if they hit their resonance frequency (critical frequencies). However, successful run-up tests in **Sec. VI** show that these critical frequencies can be passed with the present drive system. Due to the larger rotor diameter compared to the test rotor, the UCF rotor has a higher stiffness and a large reserve with respect to separation of $\mathrm{EO} = 1$ and the first bending resonance. To verify the 3D-FEM results, the test rotor was struck with a mechanical impulse while resting stationarily and the acoustic frequency response was measured with a microphone as described in [33] and is shown in **Fig. 9(c)**. The provided normalized sound pressure levels $p_{\mathrm{rel}}$ are normalized by $p_0 = 20\,\mu$Pa (calibrated at $400$ Hz with the sound pressure level measurement unit of [35]). The resonance frequencies determined acoustically and with 3D-FEM agree well, although the deviation is greater for the higher second bending mode. This can be due to the fact, that in the simulation all rotor components were modeled as firmly bonded, resulting in higher stiffness and lower damping than in the prototype with glued components. Thus, the 3D-FEM bending mode simulation was verified acoustically by experiment.

## VI. High-Speed Drive-System Test-Operation

The UCF drive system presented in this article was successfully commissioned and operated at a speed of $103\,\mathrm{krpm}$ with the test-rotor. Thus, the target speed of $100\,\mathrm{krpm}$ was reached.

In **Sec. IV-B** the appearance of parasitic induced currents due to the yoke air-gaps was predicted with the aid of 3D-FEM and analytic derivations. The experimental confirmation thereof is shown in **Fig. 10**. In **Sec. IV-E** a feed-forward control compensation was proposed. Its effectiveness is experimentally shown in **Fig. 10**. Despite the application of $L-$filters, the parasitic current was found with an amplitude of approx. $0.8\,\mathrm{A}$ at $30\,\mathrm{krpm}$ to be higher then expected from the FEM-simulations ($>\ 10\%$ of the nominal UCF operation drive current $\hat{I}_{\mathrm{q,nom}}$). This can be a consequence of the non-ideal geometry of the brittle SMC cores with broken off edges, making the interface area between the two core halves smaller then in the ideal simulation geometry. The manufacturing process should therefore be improved in the future. **Fig. 10** further shows the achieved reduction of the parasitic currents by approx. $70\,\%$ with the proposed feed-forward control scheme. Tuning of the feed-forward gain while running levitated at $30\,\mathrm{krpm}$ as shown in **Fig. 10** allowed to find the optimal gain.

The measured parasitic current amplitude of $0.8\,\mathrm{A}$ at $30\,\mathrm{krpm}$ leads to a 3D-FEM obtained cross-section average parasitic stator-core flux density component amplitude of $20\,\mathrm{mT}$. The appearance of resulting parasitic current induced loss is proven by measurement. The increase in steady state motor temperature for varying the feed-forward compensation gain from full ($100\%$) to zero and negative compensation ($-33\%$) is shown in **Fig. 11** at $20\,\mathrm{krpm}$ and $25\,\mathrm{krpm}$. It was found as predicted, that the relative motor temperature, and therefore the parasitic motor loss, grows on the one hand with reduced feed-forward compensation, and on the other hand with increasing speed.

The non-linear growth of the parasitic motor losses with speed as discussed in **Sec. IV-D** implies the necessity for this $100\,$krpm self-bearing motors to compensate the parasitic currents.

With the aid of the $L-$filter and the proposed feed-forward control method it was achieved to reduce the parasitic currents to an acceptable level despite non-ideal stator core manufacturing. With the mechanisms of the generation of the parasitic currents unveiled in this article, the doors are open to test or combine other control methods to counteract the parasitic currents. Work being reported for current regulators in active filters as reviewed in e.g. [36] could be a starting point for future investigations. Figure **Fig. 12** shows an oscilloscope screenshot of the rotor angle sensor signal measurement at $103\,\mathrm{krpm}$. Since the rotor has one pole-pair, the fundamental frequency of the shown wave-form of $1.73\,\mathrm{kHz}$ corresponds to $103\,\mathrm{krpm}$.

Having reached the target speed, implies that the critical frequencies due to higher order excitations ($\mathrm{EO} > 1$) were successfully passed. **Fig. 13** shows the radial displacement wave-forms over one rotor-revolution of the rotor angle $\vartheta$. While at $10\,\mathrm{krpm}$ some rotor vibrations are visible in **Fig. 13(a)**, at $100\,\mathrm{krpm}$ in **Fig. 13(b)** the rotor is extremely steady. **Fig. 13(c)** shows the average radial displacement radius $|\underline{x}_{\mathrm{r}}|_{\mathrm{avg}}$ for a speed run-up from $10 - 100\,\mathrm{krpm}$. Crossings of higher order excitations (**EO** $> 1$) with the test-rotor bending-modes resulted in visible displacement radius peaks. However these zones can be successfully passed with the prototype. For unrestricted long-term operation, rotor orbit radii are recommended according to standard [37] to be smaller than $30\%-40\%$ of the minimal rotor-stator clearance. With $600\,\mu\mathrm{m}$ clearance, the average rotor orbit radius during speed ramp-up $|\underline{x}_{\mathrm{r}}|_{\mathrm{avg}}$ in **Fig. 13(c)** was at resonances always below $12\%$ of the clearance. At the envisaged operating point of $100\,$krpm it was below $1\%$. Therefore this recommendation is met and the rotor vibrations sufficiently damped over the whole operating range and the drive system successfully experimentally validated.

## VII. Conclusion & Outlook

The novel magnetically double self-bearing drive system concept for ultracentrifugation with stator opening functionality for easy rotor removal and performance specifications of $100'000\,\mathrm{rpm}$ and $200'000\,\mathrm{g}$ introduced by the authors in [1] was realized as a prototype. The needed stator encapsulations provoked stator yoke air-gaps were found to lead to parasitic currents if not controlled accordingly. The usage of $L-$filters and a voltage feed-forward current control-strategy to diminish these effects was proposed and successfully implemented and tested on the newly built prototype. The working of the novel self-bearing openable stator drive-system was experimentally verified. Future work will focus on operating the system in UCF separation-mode, continuing the path towards $200'000\,\mathrm{g}$.

## Acknowledgment

The authors gratefully thank the Swiss Innovation Agency Innosuisse for their financial support and Levitronix GmbH for their financial, scientific as well as technical contributions. The authors would like to express a special thanks to Florian

This article has been accepted for publication in IEEE Transactions on Industry Applications. This is the author's version which has not been fully edited and content may change prior to final publication. Citation information: DOI 10.1109/TIA.2023.3314016

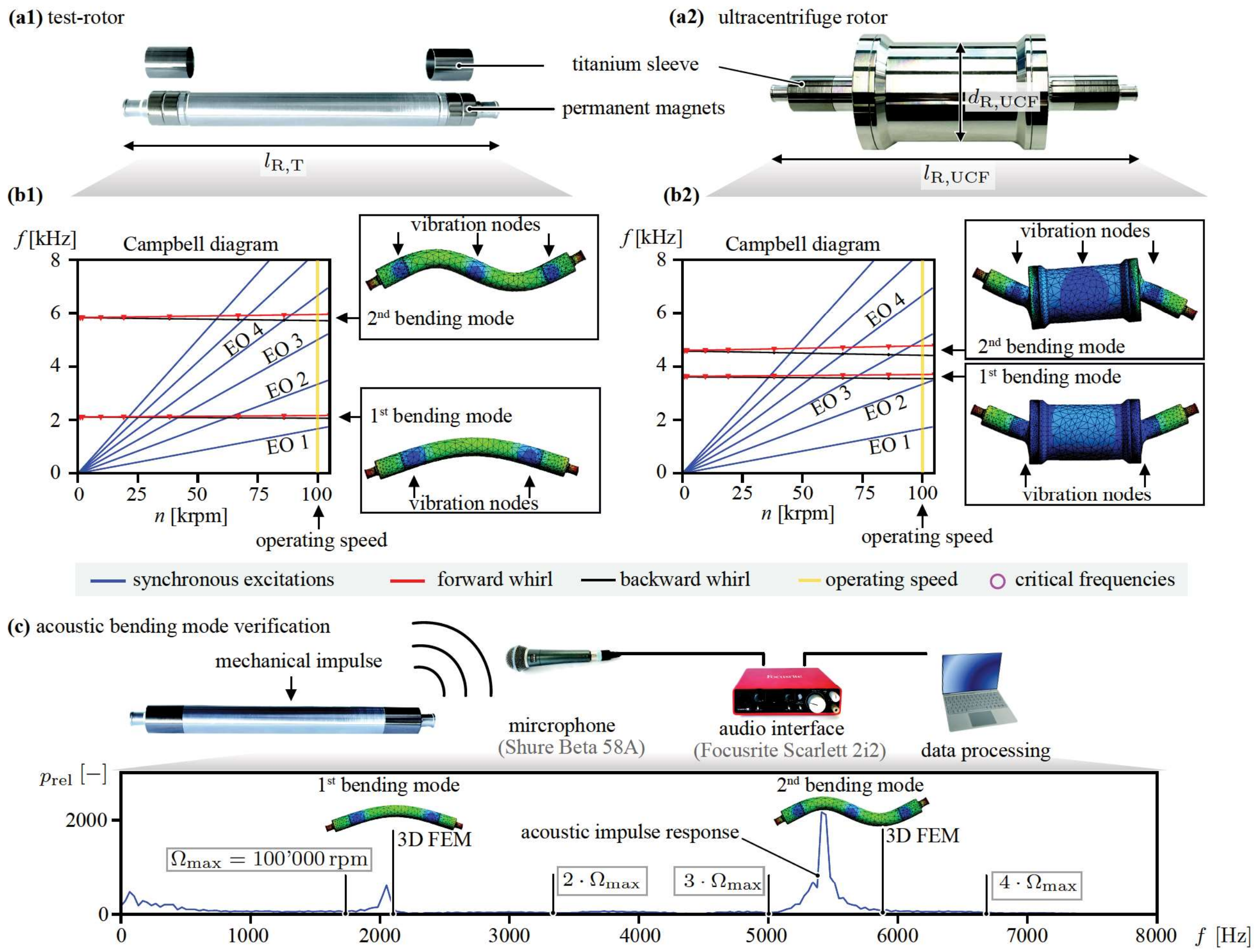


**Fig. 9:** **(a1)** Test-rotor and **(a2)** UCF rotor. **(b1)-(b2)** Corresponding 3D-FEM obtained Campbell diagrams with rotor bending modes. For both rotors, the synchronous excitation with excitation order (EO) equal to one has no intersection with the first bending mode, suggesting the absence of major vibration problems. **(c)** Acoustic impulse response measurement validation of the test-rotor bending resonance frequencies. The indicated rotor dimensions are specified in **Tab. IV**.

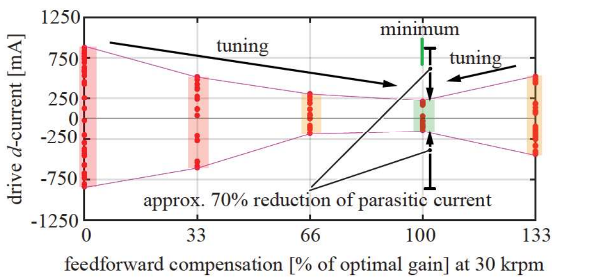


**Fig. 10:** Tuning of the parasitic induced voltage feedforward compensation gain conducted at 30 krpm and achieved drastic reduction of the parasitic currents.

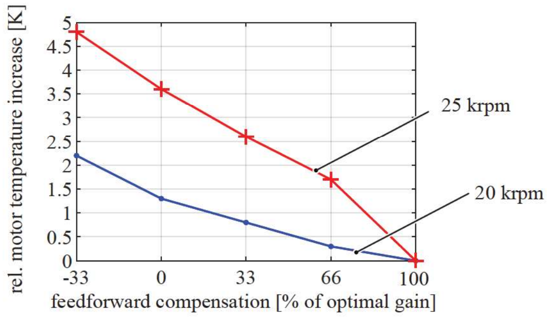


**Fig. 11:** Relative motor temperature increase for different parasitic induced voltage feed-forward compensation levels (from negative to full compensation) and two speed levels, 20 krpm and 25 krpm.

Wassmer of Levitronix GmbH for the support during the commissioning process of the novel self-bearing drive-system.

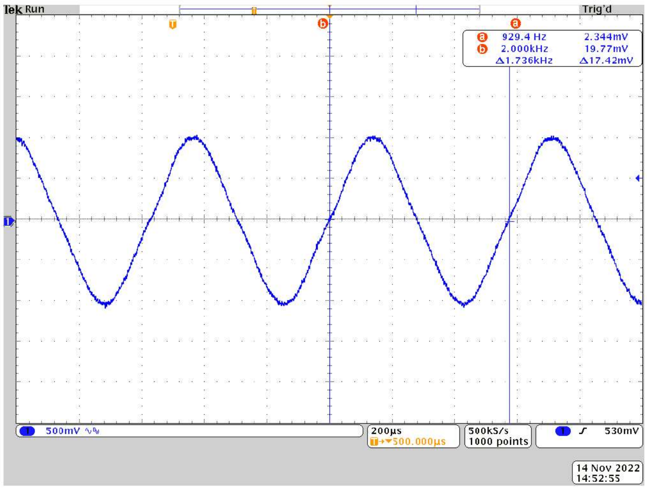

**Fig. 12:** Oscilloscope measurement of the rotor angle sensor signal (rotor number of pole pairs equal to one), as a proof of the system operation at 103 krpm.

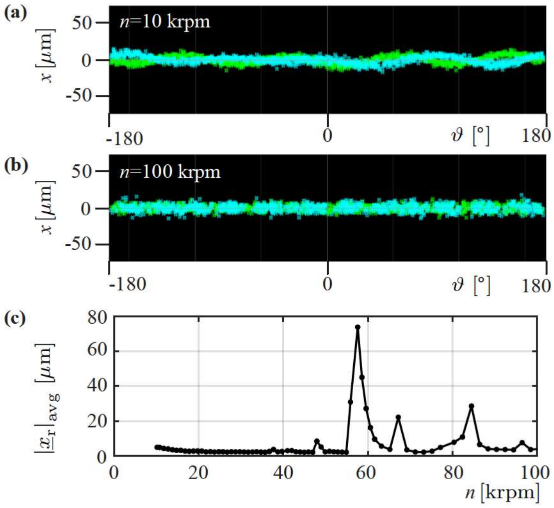


**Fig. 13:** Radial rotor displacements of both self-bearing motors over one rotor-revolution **(a)** at 10 krpm and **(b)** at 100 krpm. **(c)** Averaged radial displacement amplitude during a speed ramp-up.

## APPENDIX

**TABLE I:** System Dimensions

| *Dimension* | *Variable* | *Value* |
|---|---|---|
| System length | $l_S$ | 340 mm |
| System width | $w_S$ | 260 mm |
| System height in closed state | $h_{S,c}$ | 227 mm |
| System height in opened state | $h_{S,o}$ | 260 mm |

**TABLE II:** SBM Prototype Specifications

| *Dimension* | *Variable* | *Value* |
|---|---|---|
| Number of pole pairs | $p$ | 1 |
| Number of phases | $m_S$ | 6 |
| DC-Link voltage | $U_{DC}$ | 48 V |
| Design max. power per SBM | $P_{max}$ | 0.25 kW |
| Stator synchronous inductance | $L_S$ | 36 $\mu$H |
| Phase filter inductance | $L_F$ | 100 $\mu$H |

**TABLE III:** Drive-System Prototype Materials

| *Component* | *Material* |
|---|---|
| Stator yoke | SMC |
| Rotor PM | NdFeB |
| Rotor bodies | EN AW-7075 (AlZnMgCu1,5) |
| Rotor sleeve | Titanium |

**TABLE IV:** Rotor Dimensions

| ***Dimension*** | ***Variable*** | ***Value*** |
|---|---|---|
| Test-rotor length | $l_{\mathrm{R,T}}$ | $202\,\mathrm{mm}$ |
| Ultracentrifuge diameter | $d_{\mathrm{R,UCF}}$ | $50\,\mathrm{mm}$ |
| Ultracentrifuge length | $l_{\mathrm{R,UCF}}$ | $202\,\mathrm{mm}$ |

## REFERENCES


[1] E.J. Hubmann, C.F. Blaser, S. Erismann, D. Steinert, T. Nussbaumer and J.W. Kolar, "Magnetically Self-Bearing Drive System for Ultracentrifugation: Towards 100'000 rpm and 200'000 g," *Proc. of International Conference on Electrical Machines and Systems (ICEMS)*, pp. 88-94, 2021.

[2] M. Konrath, J. Gorenflo, N. Hübner and H. Nirschl, "Application of magnetic bearing technology in high-speed centrifugation," *Chemical Engineering Science*, vol. 147, pp. 65-73, 2016.

[3] A. Hashimoto, A. Matsui, M. Motohashi, N. Miyake, H. Ota, Y. Nakanishi and H. Nishimura, "A Novel Motor Manufacturing Technology using Spiral Type Core for Information Devices," *Proc. of JSME-IIP/ASME-ISPS Joint Conference on Micromechatronics for Information and Precision Equipment*, vol. 147, pp. 403-404, 2003.

[4] J. Chen, J. Zhu, and E.L. Severson "Review of Bearingless Motor Technology for Significant Power Applications," *IEEE Transactions on Industry Applications*, vol. 56, no. 2, pp. 1377-1388, 2020.

[5] T. Pei, D. Li, J. Liu, J. Li, and W. Kong "Review of Bearingless Synchronous Motors: Principle and Topology," *IEEE Transactions on Transportation Electrification*, vol. 8, no. 3, pp. 3489-3502, 2022.

[6] B.S. Weinreb, M. Noh, D.C. Fyler, and D.L. Trumper "Design and Implementation of a Novel Interior Permanent Magnet Bearingless Slice Motor," *IEEE Transactions on Industry Applications*, vol. 57, no. 6, pp. 6774-6782, 2021.

[7] J. Asama, and A. Chiba "Three-Coil Combined Winding Configuration for a 2-DOF Actively Controlled Bearingless Permanent Magnet Motor," *IEEE Transactions on Industry Applications*, vol. 57, no. 6, pp. 6765-6773, 2021.

[8] N.R. Hemenway, and E.L. Severson "Exact Force Vector Regulation of the Three-Pole Magnetic Bearing," *IEEE Transactions on Industry Applications*, vol. 57, no. 6, pp. 7024-7034, 2021.

[9] I. Bagaric, D. Steinert, T. Nussbaumer, and J.W. Kolar "Concept of a Novel Bearingless Three-Pole Motor for Two-Sided Driven Applications," *Proc. of International Conference on Electrical Machines and Systems (ICEMS)*, pp. 99-104, 2021.

[10] J. Asama, Y. Kamiya, and A. Chiba "Asymmetrical Four-Phase Combined Winding Arrangement for Bearingless PM Motors," *IEEE Transactions on Industry Applications*, vol. 57, no. 6, pp. 6870-6879, 2021.

[11] Z. Wen, G. Valente, A. Formentini, L. Papini, C. Gerada, and P. Zanchetta "A Novel Current Limitation Technique Exploiting the Maximum Capability of Power Electronic Inverter and Bearingless Machine," *IEEE Transactions on Industry Applications*, vol. 57, no. 6, pp. 7012-7023, 2021.

[12] T. Noguchi, H. Sugimoto, Y. Fujii, and A. Chiba "A Novel Combined Winding and Test Result of a 20-Pole/24-Slot Consequent-Pole Bearingless Motor With Parallel Motor Winding," *IEEE Transactions on Industry Applications*, vol. 57, no. 6, pp. 6880-6890, 2021.

[13] A. Khamitov, and E.L. Severson "Analysis and Design of Multi-Phase Combined Windings for Bearingless Machines," *Proc. of IEEE Energy Conversion Congress and Exposition (ECCE)*, pp. 3949-3956, 2021.

[14] A. Khamitov, W. Gruber, G. Bramerdorfer, and E.L. Severson "Comparison of Combined Winding Strategiew for Radial Nonsalient Bearingless Machines," *IEEE Transactions on Industry Applications*, vol. 57, no. 6, pp. 6856-6869, 2021.

[15] N. Petersen, A. Khamitov, T. Slininger, and E.L. Severson "Machine Design and Precision Current Regulation for the Parallel DPNV Bearingless Motor Winding," *IEEE Transactions on Industry Applications*, vol. 57, no. 6, pp. 7000-7011, 2021.

[16] D. Dietz, and A. Binder "Design Guidelines and Scaling effects for Bearingless PM Synchronous Machines Accounting for Eddy Current Reaction Filed," *IEEE Transactions on Industry Applications*, vol. 57, no. 6, pp. 6844-6855, 2021.

[17] G.B. Gallego, L. Rossini, T. Achtnich, D.M. Araujo, and Y. Perriard "Efficiency Optimization of Slotless Magnetic-Bearing Machines," *IEEE Transactions on Industry Applications*, vol. 57, no. 6, pp. 6833-6843, 2021.

[18] H. Sugimoto, and A. Chiba "Dynamic Modeling and Experimental Validations of Passing Through Critical Speeds by High Acceleration in One-Axis Actively Positioned Bearingless Motors ," *IEEE Transactions on Industry Applications*, vol. 57, no. 6, pp. 6956-6964, 2021.

[19] N. Petersen, T. Slininger, and E.L. Severson "State Observers and Run-Out Reduction for Magnetically Levitated Motor Systems," *IEEE Transactions on Industry Applications*, early access, 2022.

[20] D. Kepsu, R.P. Jastrzebski, and O. Pyrhönen, "Modeling of a 30 000 Rpm Bearingless SPM Drive With Loss and Thermal Analyses for a 0.5 MW High-Temperature Heat Pump," *IEEE Transactions on Industry Applications*, vol. 57, no. 6, pp. 6965-6975, 2021.

[21] T. Srichiangsa, H. Sugimoto, Y. Fujii, and A. Chiba, "Design, Development, and Experimental Results of a 30 000-R/Min One-Axis Actively Positioned Single-Drive Bearingless Motor," *IEEE Transactions on Industry Applications*, vol. 57, no. 6, pp. 6783-6791, 2021.

[22] J. Asama "Design of Slotless Single-Drive Bearingless Permanent Magnet Motor for High-Speed Applications," *Proc. of International Power Electronics Conference (IPEC)*, pp. 397-400, 2022.

[23] Y. Fu, S. Ogasawara, and K. Orikawa, "Investigation of Operational Characteristics and Efficiency Enhancement of an Ultrahigh-Speed Bearingless Motor at 100 000 r/min," *IEEE Transactions on Industry Applications*, vol. 56, no. 4, pp. 3571-3583, 2020.

[24] J. Asama, and A. Chiba "Performance Evaluation of a Homopolar Bearingless Motor for Ultrahigh Speed Applications," *IEEE Transactions on Industry Applications*, vol. 57, no. 6, pp. 6913-6920, 2021.

[25] P. Puentener, M. Schuck, D. Steinert and J.W. Kolar "Comparison of Bearingless Slice Motor Topologies for Pump Applications," *Proc. of International Electric Machines & Drives Conference (IEMDC)*, pp. 9-16, 2019.

[26] P. Peralta, D.M. Araujo and Y. Perriard "Design of Compact Bearingless Disc Drive Systems," *IEEE Transactions on Industry Applications*, vol. 56, no. 5, pp. 4870-4881, 2020.

[27] D. Steinert, T. Nussbaumer, J.W. Kolar "Topology Evaluation of Slotless Bearingless Motors with Toroidal Windings," *Proc. of International Power Electronics Conference (IPEC - ECCE ASIA)*, pp. 975-981, 2014.

[28] D. Steinert, T. Nussbaumer and J.W. Kolar "Slotless Bearingless Disk Drive for High-Speed and High-Purity Applications," *IEEE Transactions on Industrial Electronics*, vol. 61, no. 11, pp. 5974-5986, 2014.

[29] R. Schoeb and N. Barletta "Principle and Application of a Bearingless Slice Motor," *JSME International Journal Series C Mechanical Systems, Machine Elements and Manufacturing*, vol. 40, no. 4, pp. 593-594, 1997.

[30] Y. Okada, G. Schweitzer, and E.H. Maslen "Magnetic Bearings - Self-Bearing Motors," *Springer*, pp. 463, 2009.

[31] M.C. Kulan, N.J. Baker, K.A. Liogas, O. Davis, J. Taylor, and A.M. Korsunsky "Empirical Implementation of the Steinmetz Equation to Compute Eddy Current Loss in Soft Magnetic Composite Components," *IEEE Access*, vol. 10, pp. 14610-14623, 2022.

[32] J. Mühlethaler, J. Biela, J.W. Kolar, and A. Ecklebe "Core Losses Under the DC Bias Condition Based on Steinmetz Parameters," *IEEE Transactions on Power Electronics*, vol. 27, no. 2, pp. 953-963, 2012.

[33] "Product specifications beta 58A supercardioid dynamic vocal microphone," Shure Incorporated, 2015.

[34] A. Preumont, "Twelve Lectures on Structural Dynamics," *Springer*, pp. 87, 2013.

[35] "Data sheet testo 816-1, Sound level meter," Testo India Pvt Ltd, 2015.

[36] F. Briz, D. Diaz-Reigosa, M. W. Degner, P. Garcia, and J. M. Guerrero "Dynamic behavior of current controllers for selective harmonic compensation in three-phase active power filters," *Proc. of IEEE Energy Conversion Congress and Exposition*, pp. 2892-2899, 2011.

[37] "Mechanical Vibration - Vibration of Rotating Machinery equipped with Active Magnetic Bearings - Part 2: Evaluation of Vibration," *Standard ISO 14839-2:2004(E)*, 2004.

This article has been accepted for publication in IEEE Transactions on Industry Applications. This is the author's version which has not been fully edited and content may change prior to final publication. Citation information: DOI 10.1109/TIA.2023.3314016

**Emanuel J. Hubmann** (Student Member, IEEE) received his B.Sc. and M.Sc. degrees in mechanical engineering in 2016 and 2018, respectively, from the Swiss Federal Institute of Technology (ETH Zurich), Zurich, where he has been working toward the Ph.D. degree in advanced mechatronic systems and magnetic levitation with the Power Electronic Systems Laboratory (PES) since 2019.

He was active in organizations such as J. Wagner AG, Swiss Armed Forces, Hitachi Zosen Inova AG, BRUSA Elektronik AG, Pediatric Heart Center Department of Surgery of the University Childrens Hospital Zurich and Levitronix GmbH. His research focuses on the field of mechatronics, especially in electric drive systems and magnetic levitation for medical, biotech, and industrial applications.

Mr. Hubmann was the recipient of two Conference Prize Paper Awards and one Poster Award.

**Ricco Eberhard** received his B.Sc. degree in mechanical engineering in 2021 from the Swiss Federal Institute of Technology (ETH) Zurich. He participated in the ETH Focus Project Swissloop, where he worked towards novel, sustainable hyperloop transport, cumulating into multiple awards at the European Hyperloop Competition 2021. He did his B.Sc. thesis in cooperation with Levitronix GmbH and the Power Electronic Systems Laboratory (PES) of ETH Zurich. He is currently with Levitronix as a part-time employee, while working towards his M.Sc. degree in Mechanical Engineering at ETH Zurich.

**Christian F. Blaser** received his B.Sc. degree in mechanical engineering from the Swiss Federal Institute of Technology (ETH) Zurich in 2021 and is currently pursuing his M.Sc. degree. He worked together with Levitronix GmbH and Power Electronic Systems Laboratory (PES) of ETH Zurich during his Bachelor thesis, where he created a prototype of a magnetically levitated highspeed electric drive. Currently he is doing an internship at Suncar, a company who works in the field of electrification of construction machines.

**Stefan Erismann** received his B.Sc. and M.Sc in electrical engineering from the Swiss Federal Institute of Technology (ETH) in 2020 and 2022 respectively. During his studies he was focusing on Power Electronics and High Voltage Engineering. He was active at Stadler Rail AG as an Internship and at Levitronix GmbH during a Semester Project. Since 2022 he is working at ABB Switzerland AG in the field of Medium Voltage (MV) drives for industrial applications, such as marine or oil and gas. .

**Daniel Steinert** was born in Roth, Germany, in 1987. He received the M.Sc. degree in mechatronics from Dresden University of Technology, Dresden, Germany, in 2012, and the Ph.D. degree in bearingless motors from the Power Electronic Systems Laboratory of the Swiss Federal Institute of Technology Zurich (ETH Zurich), Zurich, Switzerland, in 2015, where he worked on high-speed bearingless motors.

He is currently with Levitronix GmbH, Zurich, Switzerland, as head of the research group where his research is focused on bearingless motor topologies, control concepts, losses, and applications of bearingless motors.

**Thomas Nussbaumer** was born in Vienna, Austria, in 1975. He received the M.Sc. (Hons.) degree in electrical engineering from Vienna University of Technology, Vienna, in 2001 and the Ph.D. degree in power electronics from the Swiss Federal Institute of Technology Zurich (ETH Zurich), Zurich, Switzerland, in 2004. From 2001 to 2006, he was with the Power Electronic Systems Laboratory, ETH Zurich, where he was involved in research on modeling, design, and control of three-phase rectifiers, power factor correction techniques, and electromagnetic compatibility. Since 2006, he has been with Levitronix GmbH, Zurich, where he is currently involved as vice president of R&D in research on bearingless motors, magnetic levitation, and permanent-magnet motor drives for the semiconductor and biotechnology industry. His current research is focused on compact and high-performance mechatronic systems, including novel power electronics topologies, control techniques, drive systems, sensor technologies, electromagnetic interference, and thermal aspects.

**Johann W. Kolar** (Fellow, IEEE) received the M.Sc. degree in industrial electronics and control engineering and the Ph.D. degree in electrical engineering (summa cum laude) from the Vienna University of Technology, Vienna, Austria.

He is currently a Full Professor and the Head of the Power Electronic Systems Laboratory at the Swiss Federal Institute of Technology (ETH) Zurich, Zurich, Switzerland.

Dr. Kolar has proposed numerous novel converter concepts incl. the Vienna Rectifier, the Sparse Matrix Converter and the Swiss Rectifier, has spearheaded the development of x-million rpm motors, and has pioneered fully automated multiobjective power electronics design procedures. He has graduated 80+ Ph.D. students, has published 1000+ journal and conference papers and 4 book chapters, and has filed 200+ patents. He has presented 30+ educational seminars at leading international conferences and has served as IEEE PELS Distinguished Lecturer from 2012–2016. He has received 40+ IEEE Transactions and Conference Prize Paper Awards, the 2014 IEEE Power Electronics Society R. David Middlebrook Achievement Award, the 2016 IEEE PEMC Council Award, the 2016 IEEE William E. Newell Power Electronics Award, the 2021 EPE Outstanding Achievement Award and 2 ETH Zurich Golden Owl Awards for excellence in teaching. He was elected to the U.S. National Academy of Engineering as an international member in 2021. The focus of his current research is on ultra-compact/efficient WBG converter systems, ANN-based design procedures, Solid-State Transformers, ultra-high speed drives, bearingless motors, and life cycle analysis of power electronic and mechatronics systems.